The Astrophysical Journal Letters, 982:L25 (9pp), 2025 March 20 https://doi.org/10.3847/2041-8213/adb8ce

Natural Generation of Alfvén Waves from Three-dimensional Bursty Interchange Magnetic Reconnection in the Solar Corona

Liping Yang[1], Jiansen He[2], Xueshang Feng[1], Daniel Verscharen[3], Fan Guo[4], Hui Li[4], Hui Tian[2], Wenya Li[5], Fang Shen[1,6], Chuanpeng Hou[2], Mijie Shi[7], Honghong Wu[8], and Ming Xiong[1,6]
[1] SIGMA Weather Group, State Key Laboratory of Solar Activity and Space Weather, National Space Science Center, Chinese Academy of Sciences, Beijing 100190, People's Republic of China; lpyang@swl.ac.cn
[2] School of Earth and Space Sciences, Peking University, 100871 Beijing, People's Republic of China; jshept@pku.edu.cn
[3] Mullard Space Science Laboratory, University College London, Surrey RH5 6NT, UK
[4] Theoretical Division, Los Alamos National Laboratory, Los Alamos NM 87545, USA
[5] State Key Laboratory of Solar Activity and Space Weather, National Space Science Center, Chinese Academy of Sciences, Beijing 100190, People's Republic of China
[6] College of Earth and Planetary Sciences, University of Chinese Academy of Sciences, Beijing 100049, People's Republic of China
[7] Shandong Key Laboratory of Optical Astronomy and Solar-Terrestrial Environment, Institute of Space Sciences, Shandong University, Weihai, 264209 Shandong, People's Republic of China
[8] School of Electronic Information, Wuhan University, 430072 Wuhan, People's Republic of China
Received 2025 January 15; revised 2025 February 15; accepted 2025 February 17; published 2025 March 19

Abstract

Alfvén waves play a significant role in solar coronal heating, solar wind acceleration, and Alfvénic turbulence formation. As a fundamental process, magnetic reconnection has long been credited as a crucial source of Alfvén waves. However, how magnetic reconnection triggers Alfvén waves remains unclear. Here, employing high-resolution simulations of three-dimensional bursty interchange magnetic reconnection in the solar corona, we unveil that Alfvén waves are spontaneously excited in the reconnecting current sheet and propagate bidirectionally, mainly along unreconnected magnetic fields. Generated by the transient reconnection events, flux ropes with enhanced total pressure persistently displace the magnetic fields in their surrounding, launching the observed large-amplitude and quasi-linearly polarized Alfvén waves, which carry substantial energy for heating the quiet corona and accelerating the solar wind. Our findings underscore the natural association between Alfvén waves and intermittent magnetic reconnection, which can be generalized to various plasma systems in astrophysical and laboratorial environments.

Unified Astronomy Thesaurus concepts: Alfvén waves (23); Solar magnetic reconnection (1504); Magnetohydrodynamical simulations (1966); Solar corona (1483)

Materials only available in the online version of record: animations

1. Introduction

Understanding the mechanisms responsible for heating the solar corona to temperatures in the millions of degrees and accelerating the solar wind to speeds exceeding hundreds of kilometers per second has been a longstanding challenge in solar physics (H. Alfvén 1947; D. E. Osterbrock 1961; W. I. Axford et al. 1999; L. Ofman 2010). Alfvén waves, characterized by their incompressible transverse oscillations along magnetic field lines, have emerged as prominent candidates for these processes (S. R. Cranmer 2012).

The existence of Alfvén waves is evidenced by in situ measurements of fluctuations in the solar wind (J. W. Belcher & J. Davis Leverett 1971; C.-Y. Tu & E. Marsch 1995). Alfvén waves are also inferred from remote-sensing observations of the solar atmosphere by line-of-sight (LOS; Doppler) velocities, the nonthermal broadening of emission lines, and swaying motions of magnetic structures in imaging data (D. Banerjee et al. 1998; B. De Pontieu et al. 2007; S. Tomczyk et al. 2007; J. He et al. 2009a; J. S. He et al. 2009b; H. Tian et al. 2012; R. J. Morton et al. 2015, 2019; Z. Yang et al. 2020b). However, despite decades of study, the mechanisms governing their generation remain elusive (T. G. Moran 2001; S. W. McIntosh et al. 2011; R. J. Morton et al. 2019).

One proposed mechanism is the excitation of Alfvén waves through magnetic reconnection, a process involving the rearrangement of magnetic field lines and the conversion of magnetic energy into other forms (A. G. Emslie & P. A. Sturrock 1982; W. I. Axford & J. F. McKenzie 1992; P. A. Sturrock 1999; C.-Y. Tu et al. 2005; L. Fletcher & H. S. Hudson 2008; S. R. Cranmer 2018). While observations of the solar atmosphere offer some support for this idea (C. E. DeForest 2004; J. W. Cirtain et al. 2007; J. He et al. 2009a; H. Tian et al. 2014), its link to Alfvén wave excitation remains uncertain. Previous numerical simulations have attempted to elucidate the relationship between magnetic reconnection and Alfvén waves (Z. W. Ma & L. C. Lee 1999; H. Kigure et al. 2010; L. C. Wang et al. 2015). However, these studies often rely on anomalous resistivity to simulate Petschek-type reconnection (H. Ji et al. 2022), and the direct correlation with velocity perturbations propagating at the Alfvén speed is lacking. In the latest 2.5D solar reconnection simulations, shear flows at boundaries induce an out-of-plane magnetic shear, facilitating the reconnection of closed and open magnetic fields (J. He et al. 2021). This reconnection results in magnetic twists and the generation of Alfvén waves, characterized by transverse velocity perturbations that propagate outward.

Moreover, 3D simulations of interchange reconnection show the transmission of twists induced by rotational motion from closed to open fields, manifesting as large-scale torsional Alfvén waves (J. K. Edmondson et al. 2009; E. Pariat et al. 2009; B. J. Lynch et al. 2014). However, disentangling the source of these waves remains challenging (P. F. Wyper et al. 2022). Consequently, the fundamental question of how Alfvén waves spontaneously arise from magnetic reconnection, particularly in bursty environments like the solar corona, persists (J. F. Drake et al. 2006; A. Bhattacharjee et al. 2009; W. Daughton et al. 2011; H. S. Fu et al. 2017; X. Cheng et al. 2018; L. Yang et al. 2020a; J. F. Drake et al. 2021).

Bursty interchange reconnection has been proposed as a significant energy driver of the fast solar wind (W. I. Axford & J. F. McKenzie 1992; L. A. Fisk 2003; C.-Y. Tu et al. 2005; L. Yang et al. 2013b; Y. M. Wang 2020; S. D. Bale et al. 2023; L. P. Chitta et al. 2023; N. E. Raouafi et al. 2023). This process involves the conversion of magnetic energy into kinetic and thermal energy, accompanied by the generation of Alfvén waves that transmit energy from the corona to the outer solar atmosphere (S. D. Bale et al. 2023; L. P. Chitta et al. 2023). Recent measurements from spacecraft such as the Parker Solar Probe and Solar Orbiter support this interpretation (S. D. Bale et al. 2023; L. P. Chitta et al. 2023).

In this study, we focus on understanding the intermittent nature of interchange reconnection in the solar corona and provide a detailed investigation into the hypothesis that reconnection serves as the source of the relevant Alfvén waves. Through high-resolution, fully 3D magnetohydrodynamic (MHD) simulation of a small-scale coronal jet, we demonstrate that a myriad of Alfvén waves are excited by bursty interchange reconnection due to the enhanced total pressure carried by the reconnected flux ropes. Our findings present compelling evidence of the missing link between reconnection and Alfvén waves.

The Alfvén waves launched in our model originate from the reconnecting current sheet and subsequently propagate bidirectionally. These waves differ from torsional Alfvén waves traveling along open fields, which result from the release of the twists within close fields through the steady interchange reconnection (B. J. Lynch et al. 2014). Additionally, our work contrasts with that of P. F. Wyper et al. (2022), who conducted a 3D large-scale simulation of the intermittent interchange reconnection in decaying active regions. They highlighted that the twists within the reconnected flux ropes can propagate along open fields as torsional Alfvén waves.

2. Modeling Setup

Our simulation solves the resistive MHD equations, with gravity, radiation loss, and thermal conduction included (L. Yang et al. 2013a, 2013b). We apply a splitting-based finite-volume Godunov-type central scheme (U. Ziegler 2004; X. Feng et al. 2011; L. Yang et al. 2013b), in which the approximate Riemann solver with Harten–Lax–van Leer discontinuities is used to calculate numerical fluxes, and the constrained transport algorithm is implemented to ensure the divergence-free state of the magnetic field.

The computational volume spans a box of approximately $(0,\ 0,\ 0)\,\mathrm{Mm} \leqslant (x,\ y,\ z) \leqslant (80,\ 80,\ 80)\,\mathrm{Mm}$ (where $z = 0$ represents the solar coronal base). We resolve the computational volume by a block-structured grid with adaptive mesh refinement, which is designed to automatically capture with the highest resolution the reconnecting structures and the waves (L. Yang et al. 2013a, 2015). During the calculation, we apply the highest resolution at any location with $|\boldsymbol{j}|/(|\boldsymbol{B}| + \epsilon) > \varsigma\tau$, where τ is the rms value for $|\boldsymbol{j}|/(|\boldsymbol{B}| + \epsilon)$ in the full domain, $\epsilon = 1 \times 10^{-10}$, and ς is delicately tuned to be about 15. We also refine any location where the excited Alfvén waves propagate. With these settings, seven levels of grid refinement are used to obtain a grid cell size of about 31 km in the regions of the reconnection and the waves.

We initialize the plasma as a stratified atmosphere with a uniform temperature of $T = 2 \times 10^6\,\mathrm{K}$ and a density $\rho = \rho_i \exp(-zg/RT)$, where $\rho_i = 2 \times 10^{-12}\,\mathrm{kg\,m^{-3}}$ and R is the gas constant. The plasma is in hydrostatic equilibrium with a constant value of the solar gravitational acceleration g. The initial magnetic field is a superposition of a uniform vertical background field with $\sim 10^{-3}$ T and a closed loop generated by an infinite straight-line current positioned below the bottom boundary. Such initial conditions are configured to simulate coronal interchange reconnection with a low plasma β (the ratio of gas pressure to magnetic pressure) of about 0.1. In the reconnection region, the Alfvén speed is about $500\,\mathrm{km\,s^{-1}}$, and the Lundquist number is about 4×10^5.

At the bottom boundary ($z = 0$), we impose a horizontal flow to energize the MHD system (L. Yang et al. 2013a, 2013b, 2018). The horizontal flow is prescribed as $v_x(x, y, z = 0) = 8 \times (1 - \exp(-(x - x_0)^2)) \times (1 + \tanh(x - x_0))\,\mathrm{km\,s^{-1}}$, where x_0 is the x offset of the loop's right footpoint. This subsonic and highly sub-Alfvénic flow leads to a slow squeezing of the loop by the convected open field lines in the horizontal plane, so that the loop expands vertically. As a result, the current sheet between the loop and the open fields becomes thin, and bursty reconnection is triggered. The other boundaries of the simulation domain are set to be open, so that plasma and the magnetic flux can enter or exit freely (C. Shen et al. 2022).

Based on the 3D MHD data, we calculate the specific intensity I for the Fe XV 284 Å spectral line along a predefined LOS direction with the FoMo code (T. Van Doorsselaere et al. 2016). We use the CHIANTI database (K. P. Dere et al. 1997) to get the contribution function for Fe XV by assumptions of a coronal abundance and an ionization equilibrium. We select the LOS direction along the y-axis, where the Alfvén wave perturbations are most pronounced. The first and second moments of the emission line profiles yield the Doppler velocities and line widths.

The singular value decomposition (SVD) method is employed to resolve the frequencies and wavevectors of the waves by identifying the wavevector direction $\boldsymbol{k}$ such that $S\cdot\boldsymbol{k} = 0$, where $S_{ij} = \langle \tilde{B}_i \tilde{B}_j^* \rangle$ is the spectral tensor, and $\tilde{\boldsymbol{B}}$ is the Fourier transform or wavelet transformation of the magnetic field $\boldsymbol{B}$ (O. Santolík et al. 2003; L. L. Zhao et al. 2022). Considering $\boldsymbol{k}$ as real-valued, the condition can be rewritten as $\boldsymbol{A}\cdot\boldsymbol{k} = 0$, where $\boldsymbol{A}$ is the spectral matrix. We apply wavelet analysis to the magnetic field (L. Yang et al. 2017) and obtain a time t and period p dependent spectral matrix $\boldsymbol{A}(t, p)$. The envelope of the Morlet wavelet function is used to calculate the local mean magnetic field $\boldsymbol{B}_0$. Based on the divergence-free requirement of the magnetic field, we determine the three singular values of the spectral matrix $\boldsymbol{A}(t, p)$. The wavevector $\boldsymbol{k}(t, p)$ is estimated by the eigenvector that is relevant to the smallest singular value $\lambda_1(t, p)$. The wave propagation angle $\theta_{\boldsymbol{k},\boldsymbol{B}_0}$ is defined as the angle between $\boldsymbol{k}(t, p)$ and $\boldsymbol{B}_0$. The sense

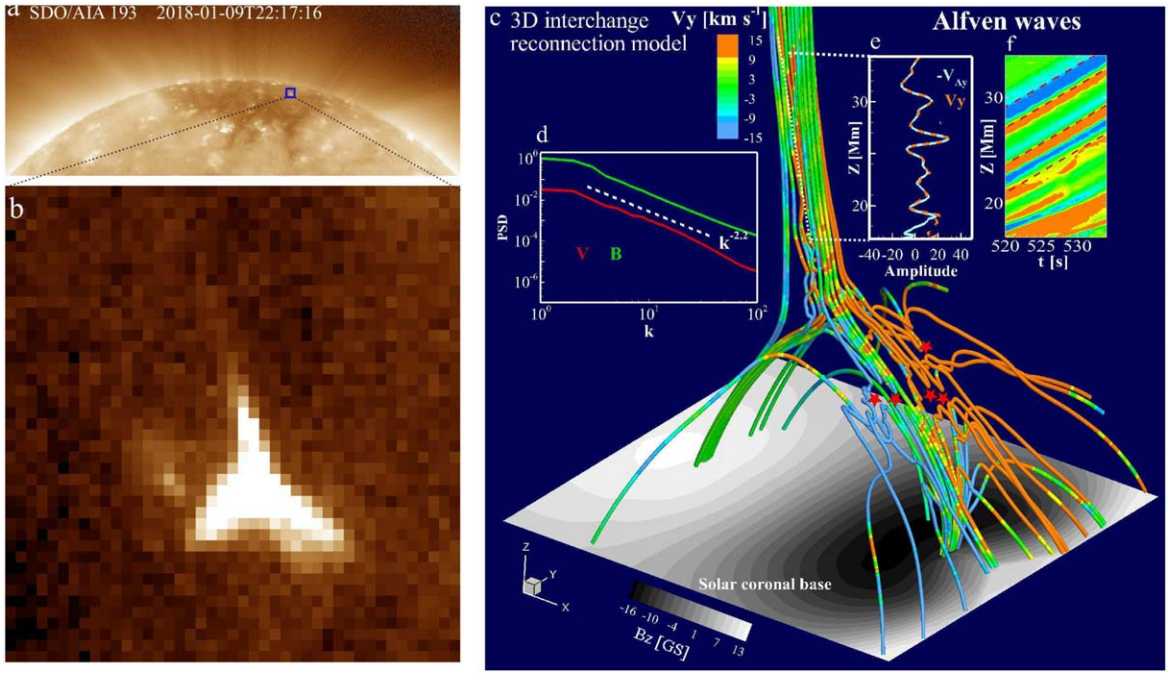

Figure 1. Observations and 3D modeling of interchange reconnection in the solar corona. (a) Solar Dynamics Observatory/Atmospheric Imaging Assembly 193 Å image of the polar coronal hole on 2018 January 9, showing many bright points and jets. (b) Enlarged view of the jet marked by the blue square in panel (a). (c) 3D view of magnetic field lines and excited Alfvén waves at $t = 534.5$ s. Here, the colored rods represent magnetic field lines, and the colors denote the values of the velocity component, V_y. The red stars mark possible reconnection sites. (d) Energy spectra of the velocity $\boldsymbol{V}$ (red line) and the magnetic field $\boldsymbol{B}$ (green line), which display power-law profiles. (e) Variations of the velocity component V_z (orange curve) and the Alfvén velocity component $-V_{Ay}(=-B_y/\rho^{0.5})$ (cyan curve) along the white line in panel (c). (f) The distance–time evolution of V_y along the white line in panel (c), with the red dashed lines showing the propagating speed.

of magnetic polarization about $\boldsymbol{B_0}$ is estimated as $\lambda_3(t, p)/(\lambda_1(t, p) + \lambda_2(t, p) + \lambda_3(t, p))$, with $\lambda_2(t, p)$ being the intermediate singular value and $\lambda_3(t, p)$ the largest singular value. The ellipticity of the polarization is calculated as $\chi = \lambda_2(t, p)/\lambda_3(t, p)$. Assuming that $\lambda_1 \ll \lambda_2$, circular polarization is characterized by χ approaching 1, and linear polarization by χ close to 0.

3. Results

The simulation is designed to model the bursty interchange reconnection between a closed loop and nearby open fields, which mimics a typical configuration of solar coronal jets (see Figures 1(a) and (b) for examples). Figure 1(c) gives a 3D view of magnetic field lines, which shows that open field lines are convected toward closed field lines, resulting in a cusp structure like the solar coronal jet shown in Figure 1(b). Regions with very low field strengths (e.g., X-point-like configurations) are the main candidate locations where the reconnection occurs (marked by red stars). Some reconnected field lines trace out in twisted geometric configurations, which are features of magnetic flux ropes. Both the velocity and the magnetic field fluctuations exhibit a power-law spectrum with an index of about −2.2 (Figure 1(d)), in accordance with the scaling in the plasmoid-mediated turbulence (e.g., S. Boldyrev & N. F. Loureiro 2017; A. Mallet et al. 2017; L. Comisso et al. 2018).

A new feature resolved in our simulation is the wavelike signals of the velocity component, V_y, that also modulate the frozen-in field lines in Figure 1(c). In our case, the background magnetic field aligns closely with the z-axis at $z > 20$. After background detrending, Figure 1(e) shows that the variation of the perpendicular perturbation V_y along the z-axis is almost equal to $-V_{Ay}(=-B_y/\sqrt{\mu_0\rho}$, with μ_0 being magnetic permeability) at $z > 20$, manifesting that V_y and V_{Ay} satisfy the polarity relation of Alfvén waves. Figure 1(f) further shows that perturbations in V_y propagate along the z-axis at the Alfvén speed V_{Az}. This evidences that the wavelike signals in V_y are signatures of Alfvén waves, which are launched by the reconnection process.

Figures 2(a)–(e) show the motion of the postreconnection fields. At $t = 522.55$ s, the newly reconnected fields primarily lie in the x−z plane. Alfvén waves are visible in the form of variations of B_y along these fields. Convected with the reconnection outflow, the newly reconnected fields and the Alfvén waves move upward and enter the reconnection outflow region (at $t = 522.80$ s and $t = 523.05$ s). Therein, the reconnected fields with the Alfvén waves overshoot, forming magnetic switchbacks. By $t = 523.20$ s, the switchbacks develop, and by $t = 523.95$ s, the switchbacks relax. Meanwhile, we observe a driven jet with a velocity of about 200 km s^{-1}, as well as the propagation of the Alfvén waves in the driven jet.

Figures 2(f)–(i) and the animations show that based on the negative correlation between V_{Ay} (2f) and V_y (2h), the Alfvén waves with an amplitude of about 20 km s^{-1} originate in the reconnecting current sheet. Following their generation, they travel bidirectionally, mainly along the fields in the inflow regions, with one group of the waves ascending into the higher solar atmosphere and the other descending into the lower solar atmosphere.

Based on the simulation results, we now estimate observable signatures of this process. Figures 2(j)–(m) and the animations present synthesized Doppler velocities and line widths for Fe XV 284 Å at the Multi-slit Solar Explorer (MUSE)'s resolution.

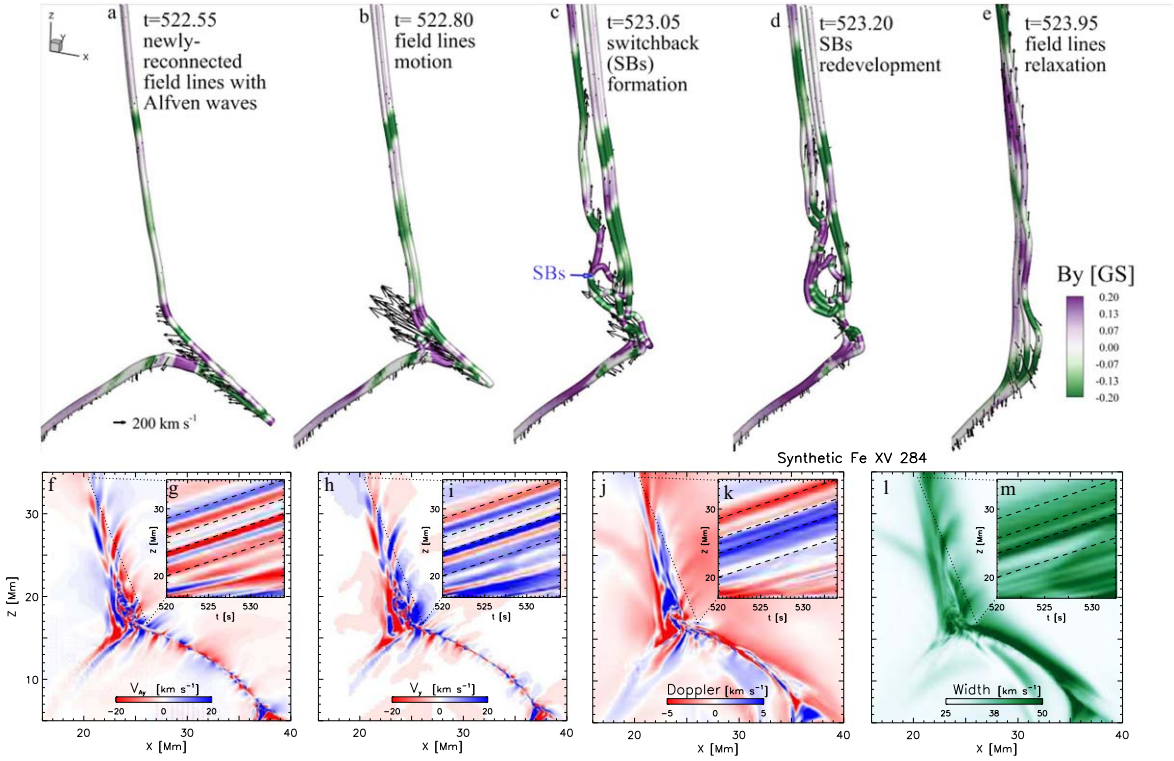

Figure 2. Alfvén waves generated by interchange magnetic reconnection in the solar corona. (a)–(e) 3D view of reconnected magnetic field lines at different times. Here, the colored rods represent magnetic field lines with the colors denoting the values of the magnetic field component, B_y. The black arrows indicate plasma flow velocities. (f), (h) 2D slice in the $x-z$ plane of the 3D model at $t = 528.0$ s, in which the colors stand for V_{Ay} and V_y. (j), (l) Plane-of-sky images of Doppler velocities (Doppler) and line widths (Width) for Fe XV 284 Å at MUSE's resolution at $t = 528.0$ s. (g), (i), (k), (m) Distance–time evolution of V_{Ay}, V_y, Doppler, and width along the black dotted line in panels (f)–(l), with the black dashed lines showing the propagating speed. The temporal evolutions of V_{Ay}, V_y, Doppler, and width are shown in the animations. Panels (f), (h), (j), and (i) are accompanied by an animation that presents the evolution processes of V_{Ay}, V_y, Doppler, and width from $t = 520.0$ s to $t = 534.0$ s with a duration of 0.25 s.

(An animation of this figure is available in the online article.)

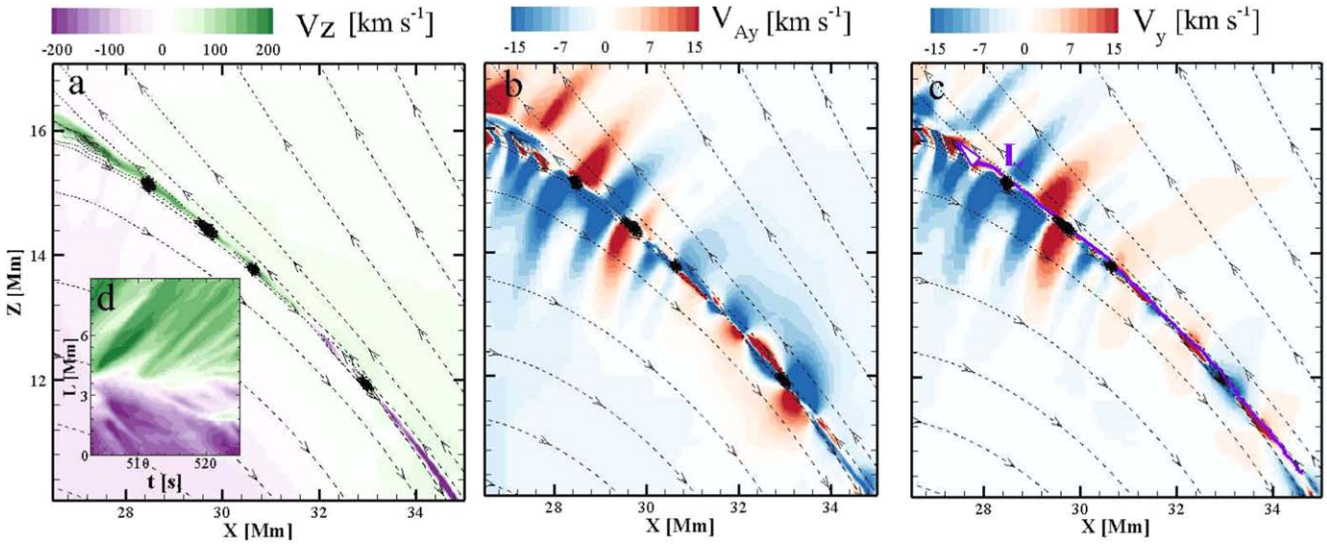

Figure 3. Bursty reconnection with Alfvén waves. (a)–(c) Distributions of the velocity component V_z, the Alfvén velocity component V_{Ay}, and the velocity component V_y in the $x-z$ slice at $t = 523.5$ s. Here, the arrowed black dashed lines represent magnetic field lines. (d) Distance–time evolution of V_z along the purple line in panel (c). Panels (a), (b), and (c) are accompanied by animations that present the evolution processes of V_z, V_{Ay}, and V_y from $t = 503.0$ s to $t = 525.0$ s with a duration of 0.25 s.

(An animation of this figure is available in the online article.)

We observe the evident signals of Alfvén waves as well as their propagation.

To gain insight into the generation of Alfvén waves during reconnection, Figure 3 and the animations provide a magnified view of the reconnecting region in an x–z slice. This reveals plasmoid-like chains with spiraled magnetic field lines and a primary reconnection X-point, which produces bidirectional intermittent outflows. As the animations of Figure 3

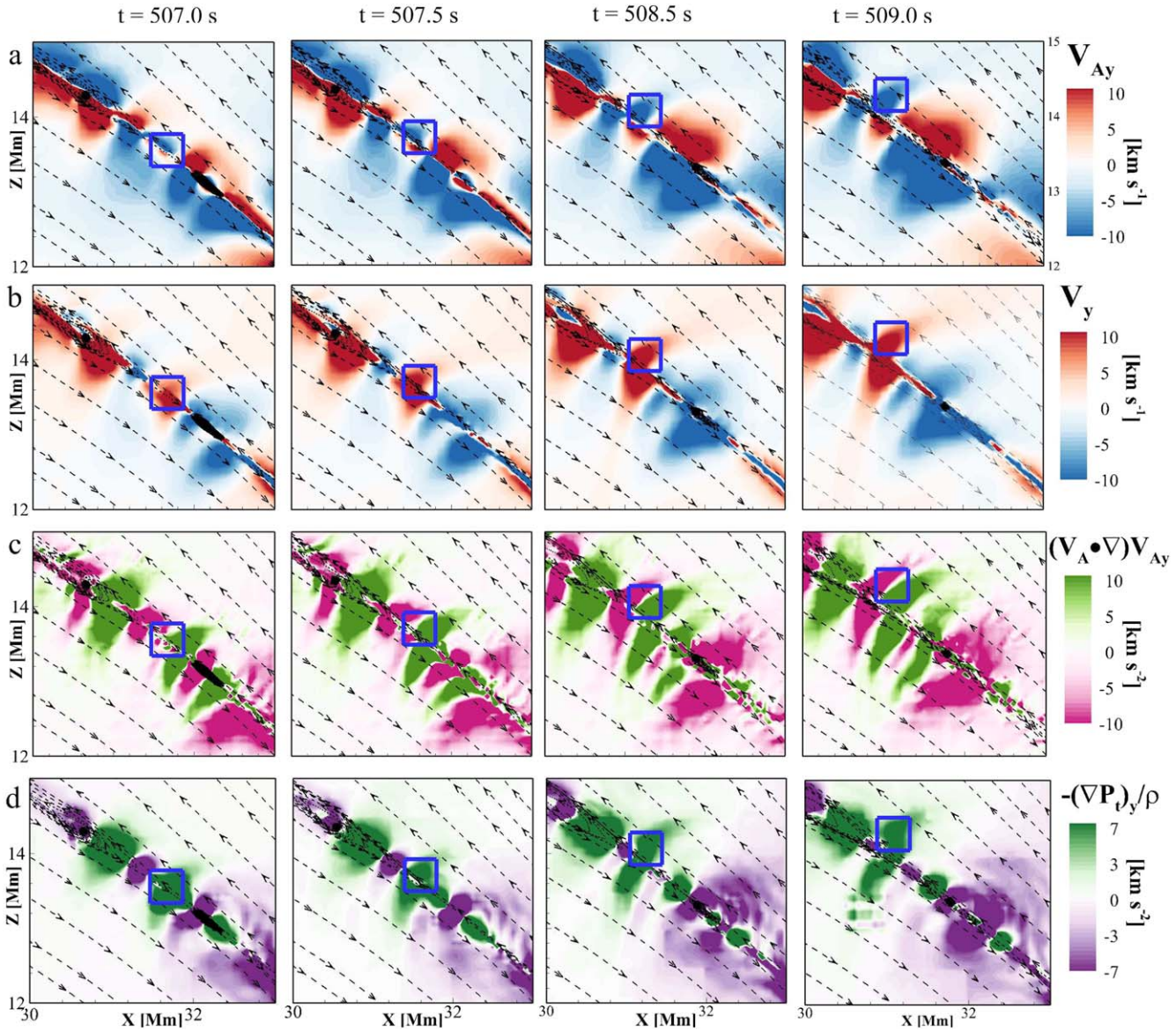

Figure 4. Development of an Alfvén wave packet in the reconnecting current sheet. (a)–(d) Distributions of the Alfvén velocity component V_{Ay}, the velocity component V_y, the discretized y-component of the magnetic tension force $(\boldsymbol{V_A}\cdot\nabla)V_{Ay}$, and the discretized y-component of the total pressure gradient force $-(\nabla P_t)_y/\rho$ in a subregion of the $x-z$ slice. The blue square highlights the Alfvén wave packet. The black dashed lines represent the magnetic field lines, with arrows denoting the direction of the magnetic field.

demonstrate, the plasmoid-like chains form repeatedly, and the outflows are emitted through a bursty reconnection process. Concurrently, Alfvén waves occur on both sides of the reconnecting current sheet, characterized by a negative correlation between V_{Ay} and V_y (Figures 3(b) and (c)). The animations of Figure 3 further showcase the constant excitation of Alfvén waves, with wavefronts traversing the unreconnected magnetic fields.

Figure 4 details the evolution of an Alfvén wave packet within and around the reconnecting current sheet. Initially, at $t = 507.0$ s, an anticorrelation between V_y and V_{Ay} emerges, marked by a blue square. These signals intensify by $t = 507.5$ s and subsequently expand into the inflow region from $t = 508.5$ s to $t = 509.0$ s. As they propagate upward along the magnetic fields in the inflow region at the Alfvén speed, accompanied by the anticorrelation between V_y and V_{Ay}, an Alfvén wave packet is formed. To investigate the origin of this wave packet, we consider the following equation derived from the y-component of the momentum equation (E. Marsch & A. Mangeney 1987):

$$\frac{\partial V_y}{\partial t} - (\boldsymbol{V_A}\cdot\nabla)V_{Ay} = -\frac{1}{\rho}(\nabla P_t)_y - (\boldsymbol{V}\cdot\nabla)V_y - V_{Ay}(\nabla\cdot\boldsymbol{V_A}), \quad (1)$$

where the Alfvén velocity $\boldsymbol{V_A} = \boldsymbol{B}/\sqrt{\mu_0\rho}$. The terms on the left-hand side reflect the propagation of V_y disturbances at the Alfvén speed when $V_y = \pm V_{Ay}$ for Alfvénic fluctuations, while the three terms on the right-hand side are due to pressure gradient, advection, and density fluctuations, respectively. By comparing the magnitudes of the right terms, we identify which term has the dominant influence on wave propagation. Figures 4(c) and (d) analyze the discretized y-component of the magnetic tension force $(\boldsymbol{V_A}\cdot\nabla)V_{Ay}$ and the total pressure gradient force $-(\nabla P_t)_y/\rho$. $(\boldsymbol{V_A}\cdot\nabla)V_{Ay}$ facilitates the

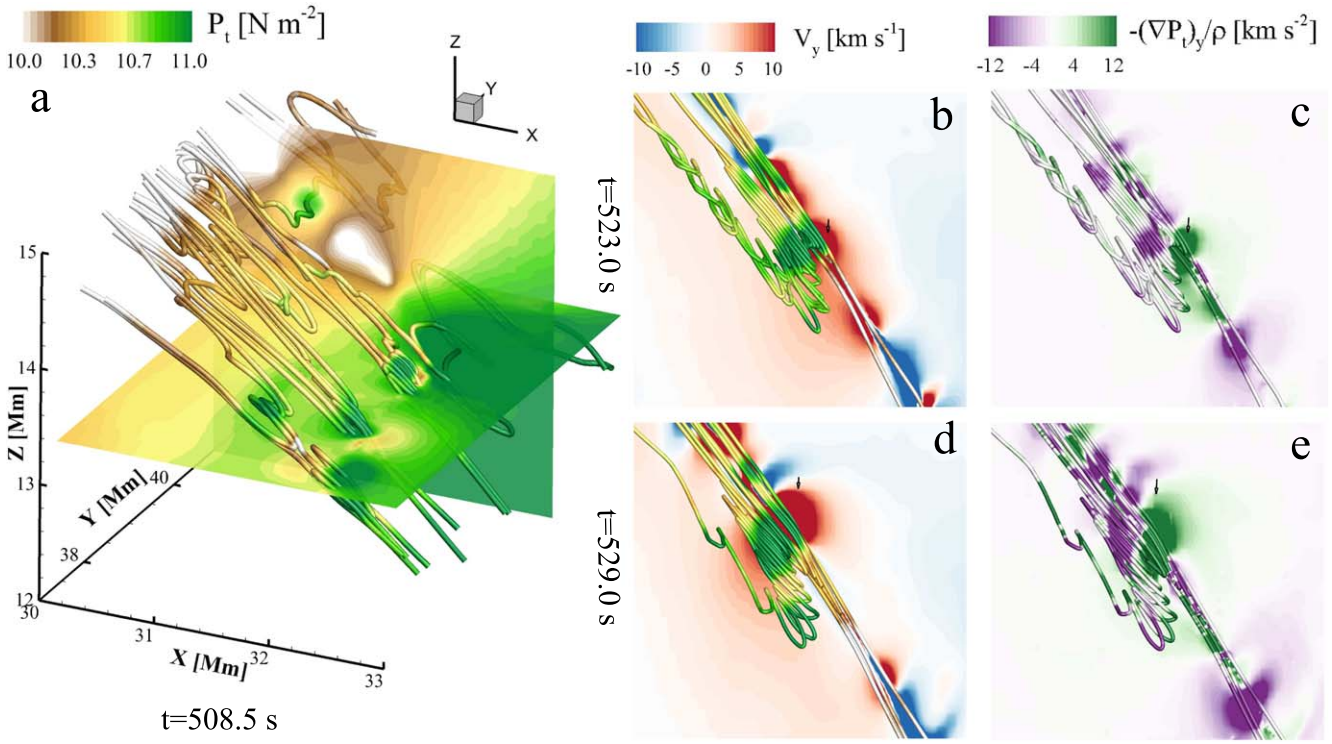

Figure 5. Flux ropes and their generation of Alfvén waves. (a) Configurations of magnetic field lines (colored rods) in the reconnecting current sheet. Colored planes show 2D slices in the $x-z$ and $x-y$ planes at $t = 508.5$ s, with colors representing total pressure, P_t. (b)–(e) 3D view of a flux rope and its generation of an Alfvén wave packet at $t = 523.0$ s and $t = 529.0$ s. Colors on the slice represent the values of V_y (b, d) and the discretized y-component of the total pressure gradient force $-(\nabla P_t)_y/\rho$ (c, e). Panel (b) is accompanied by an animation that presents the temporal evolution of the flux rope and its generation of the Alfvén wave packet from $t = 521.0$ s to $t = 533.0$ s with a duration of 0.13 s.

(An animation of this figure is available in the online article.)

propagation of V_y along the field at the Alfvén speed, while $-(\nabla P_t)_y/\rho$ significantly contributes to the evolution of V_y.

To interpret the origin of the large contribution from $-(\nabla P_t)_y/\rho$, we examine the states of plasma and magnetic fields in the reconnecting current sheet. Flux ropes, which are generated by bursty reconnection, have a stronger total pressure than their surroundings (Figures 5(a), (b), and (d)). The enhanced total pressure of the flux ropes exerts a significant gradient force on the plasma surrounding the flux ropes. When this force is perpendicular to the magnetic fields, it drives a transverse perturbation of plasma (Figures 5(b)–(e) and the animation). The magnetic frozen-in effect causes this perturbation to displace the magnetic field lines transversely, resulting in Alfvén waves.

Moreover, the bursty reconnection ejects the flux ropes at the Alfvén speed, which indicates that the kinematic speed of the flux ropes closely matches the propagation speed of the Alfvén waves. As a result, the movement of the flux ropes keeps pace with the traveling of the Alfvén waves generated by them, which provides an opportunity for the flux ropes to persistently build up the velocity pertubation of the Alfvén waves, thus making the Alfvén waves grow and spread.

The energy carried by Alfvén waves is essential for their role in heating the solar corona and accelerating the solar wind. We calculate the energy flux of the Alfvén waves $F_{\rm wy} = \rho \delta V_y^2 V_{\rm A}$, where δV_y denotes the perturbations of the Alfvén waves. In Figure 6(a) the energy flux carried by the Alfvén waves is on the order of $100\,{\rm W\,m^{-2}}$, with the maximum reaching approximately $1000\,{\rm W\,m^{-2}}$, which exceeds the required energy flux of $\sim 100\,{\rm w\,m^{-2}}$ for local heating of the quiet solar corona and solar wind acceleration (B. De Pontieu et al. 2007). The amplitudes of the waves, estimated through rms values of δV_y, range from 2 to $80\,{\rm km\,s^{-1}}$, averaging around $30\,{\rm km\,s^{-1}}$ (Figure 6(b)).

Figures 6(c) and (d) show that along the funnel fields, primarily in the z-direction, the polarization direction of the Alfvén wave velocity perturbations is in both the y- and x-directions. Perturbations in speed parallel to the funnel fields (δV_z) correlate well with density perturbations ($\delta\rho$), suggesting the presence of upward slow-mode waves (Figure 6(e)).

Detailed analysis of the wave features in Figures 6(c)–(e) is presented in Figures 6(f)–(i). Applying SVD to the temporal magnetic field variations at the red dot in Figure 6(a) (O. Santolík et al. 2003), we find that the waves mainly propagate along the mean magnetic field (small $\theta_{\boldsymbol{k},\boldsymbol{B_0}}$, Figure 6(f)) with transverse magnetic oscillations (large $\theta_{\delta\boldsymbol{B},\boldsymbol{B_0}}$, Figure 6(g)), confirming the presence of Alfvén waves. The waves have a period of a few seconds, and the polarization of the Alfvén waves is mixed, with both right-hand and left-hand polarities (Figure 6(h)). The net ellipticity is close to 0 (Figure 6(i)).

4. Summary and Discussion

We have conducted a fully 3D MHD simulation of bursty interchange reconnection in the solar corona that successfully launches Alfvén waves carrying the energy flux required for local coronal heating and solar wind acceleration. In our 3D geometry, the plasma and magnetic field in the reconnecting current sheet exhibit inhomogeneities perpendicular to the reconnection plane, which create transverse perturbations that propagate away as the Alfvén waves. The flux ropes, ejected by

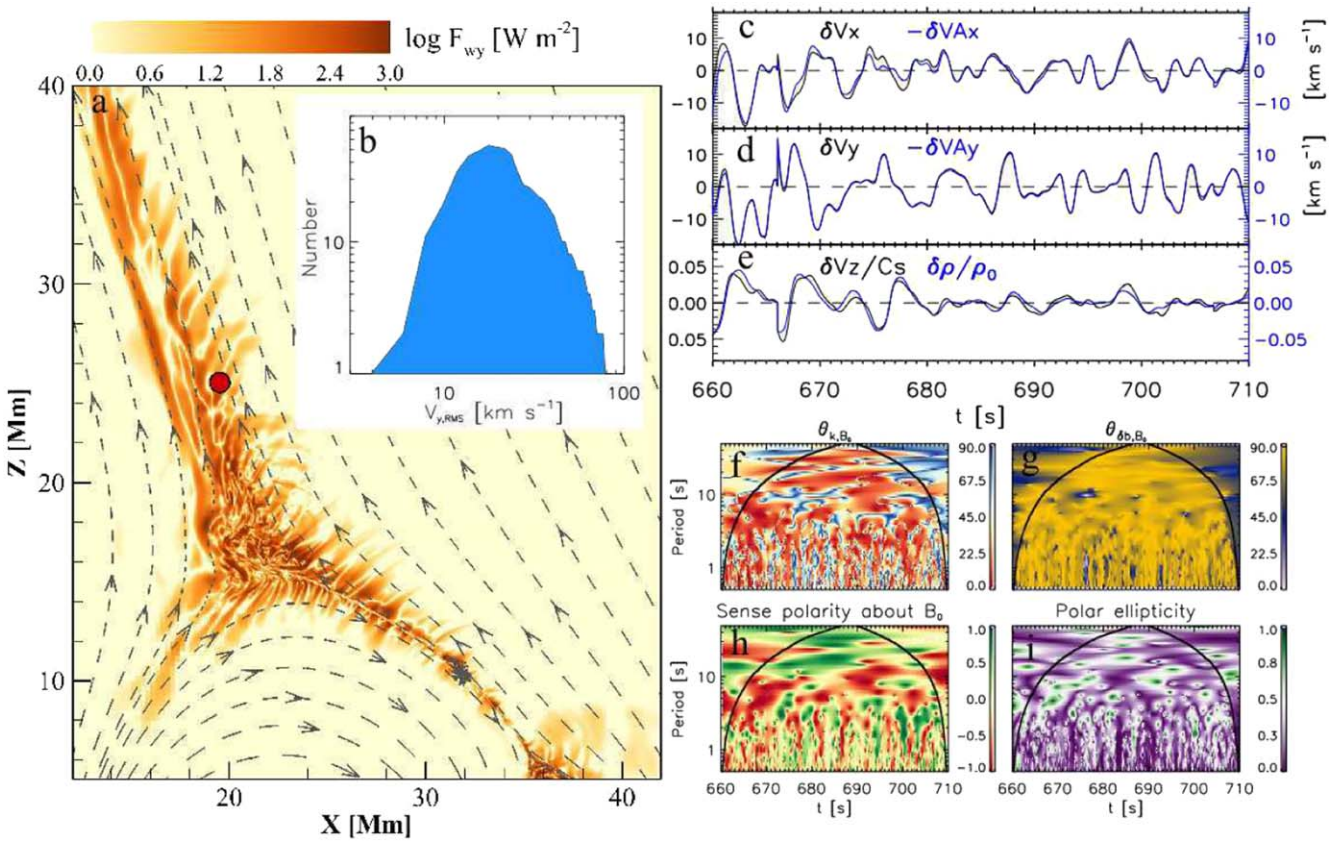

Figure 6. Properties of the Alfvén waves launched by interchange reconnection in the solar corona. (a) Wave energy flux $F_{\rm wy}$ in the x–z slice at $t = 665.0$ s. Gray dashed lines represent magnetic field lines, with arrows indicating the field direction. (b) The rms values of V_y in the x–z slice. (c)–(e) Temporal variations of the perturbed velocity components (δV_x and δV_y, black lines); the negative perturbed Alfvén velocity components ($-\delta V_{\rm Ax}$ and $-\delta V_{\rm AyAy}$, blue lines); $\delta V_z/C_s$, with C_s being sonic speed and calculated by the mean thermal pressure and the mean density (black line); and $\delta\rho/\rho_0$, with ρ_0 being the mean density (blue line) at the point of $x = 19.5$ Mm, $y = 40.0$ Mm, and $z = 25.0$ Mm (the red dot in panel (a)) on the wave path. (f)–(g) Spectra of the angle between the wavevector $\boldsymbol{k}$ and the local mean magnetic field $\boldsymbol{B_0}$ ($\theta_{\boldsymbol{k},\boldsymbol{B_0}}$, $\boldsymbol{f}$) and the angle between the perturbed magnetic field $\delta\boldsymbol{B}$ and $\boldsymbol{B_0}$ ($\theta_{\delta\boldsymbol{B},\boldsymbol{B_0}}$, $\boldsymbol{g}$). (h) The sense of magnetic polarization about $\boldsymbol{B_0}$ with the values of -1 and $+1$ denoting the left-hand and right-hand circular polarization. (i) Ellipticity of the polarization, where 0 represents linear and 1 represents circular polarization. The black curve in panels (f)–(i) shows the profile of the cone of influence of the wavelet transform.

intermittent reconnection and characterized by enhanced total pressure, are instrumental for the triggering of the Alfvén waves.

Although the concept of reconnection exciting Alfvén waves has been proposed for decades (W. I. Axford et al. 1999), our simulations provide the first concrete evidence within a realistic 3D solar corona context. Our model is different from models in which Alfvén waves arise from the relaxation of reconnected field lines with highly curved geometries (M. Mathioudakis et al. 2013). It is also distinct from the Alfvén wave origin in Petschek-like reconnection, where Alfvén waves exist in the form of rotational discontinuities standing in the flow field so as to twist the magnetic field on both sides of the field reversal region (H. E. Petschek & R. M. Thorne 1967; V. M. Vasyliunas 1975).

Our results have significant implications for solar coronal observations. While there is some evidence for transverse waves in the lower solar atmosphere (C. E. DeForest 2004; A. Keiling 2024), current solar coronal observations predominantly capture transverse waves with lower frequency than those predicted by our simulations due to the limitations of instrumentation's spatial and temporal resolution (B. De Pontieu et al. 2007; S. Tomczyk et al. 2007; S. W. McIntosh et al. 2011; R. J. Morton et al. 2019). Our findings support the existence of smaller-scale, shorter-period transverse waves in the solar corona that could be detected by future missions equipped with high-sensitivity and high-cadence diagnostics, such as the MUSE mission (Figure 2 and the animations).

Our model underscores that Alfvén waves are intrinsically linked to reconnection, and suggests that their combined action may contribute to coronal heating and solar wind acceleration (W. I. Axford & J. F. McKenzie 1992; C.-Y. Tu et al. 2005; S. W. McIntosh et al. 2011; S. R. Cranmer 2018). The first stage of this combined process involves initial plasma ejection and heating of plasma through magnetic reconnection. This is followed by a second stage of wave dissipation that further energizes the plasma. Our model also produces downward-propagating waves, which may be an important source of counterpropagating wave packets as required for the production of a turbulent cascade (B. D. G. Chandran et al. 2009). The downward-propagating waves can also be responsible for heating in the lower solar atmosphere. Given the likelihood of intermittent magnetic reconnection occurring in other magnetized stars, reconnection-driven Alfvén waves could play a pivotal role in energizing stellar coronae across the cosmos.

It is particularly noteworthy that our simulation of the 3D intermittent reconnection independently reproduces a power-law spectrum of approximately $k^{-2.2}$ for both the velocity and magnetic field fluctuations, where k denotes the wavenumber. This spectral scaling aligns with those observed in previous

simulations of the plasmoid-mediated turbulence (e.g., Y.-M. Huang & A. Bhattacharjee 2016; C. Dong et al. 2022). These findings warrant further investigation into the statistical properties of this turbulent regime.

Another aspect to consider is that our simulation has successfully generated switchbacks within the outflow region of the interchange reconnection. Nevertheless, these switchbacks do not propagate away from the Sun at the Alfvén speed. Once the switchbacks are far away from the outflow region, their magnetic fields tend to straighten. In future research, we will explore whether the constant magnetic pressure in the low plasma beta corona causes the generated switchbacks to relax, as suggested by L. A. Fisk & N. A. Schwadron (2001) and A. Tenerani et al. (2020). Given that our computational domain extends only up to about 80 Mm in the vertical direction, our current simulation cannot either rule out or confirm whether the large-amplitude Alfvén waves or the high-speed jet resulting from the interchange reconnection are responsible for the switchbacks observed by the Parker Solar Probe, as demonstrated by A. Mallet et al. (2021), C. Hou et al. (2024), and J. Touresse et al. (2024). We plan to expand our computational domain into a spherical wedge to study the radial evolution of the large-amplitude Alfvén waves and the high-speed jet seeded by the interchange reconnection, as well as their connections to the switchbacks and the solar wind.

Our simulation shares some similarities and differences with the interchange reconnection model for the generation of switchbacks proposed by G. P. Zank et al. (2020). In the model of G. P. Zank et al. (2020), the interchange reconnection between open fields and a large coronal loop with a characteristic height of about 6 *Rs* (*Rs* is the solar radius) launches the nominal switchback, with one propagating upward and the other downward toward the solar surface. Meanwhile, the hot tenuous plasma from the loop is released into the open fields, most likely in the form of a jet. In our simulation, the coronal loop has a height of only about 20 Mm, and the plasma within the loop maintains the same state as that in the open fields. The switchbacks generated by the model of G. P. Zank et al. (2020) are expected to be compressible complex structures propagating at the fast magnetosonic speed, which will constitute our future research target.

Finally, S. D. Bale et al. (2023) and J. F. Drake et al. (2023) presented a picture in which interchange reconnection heats the ambient coronal plasma and ejects the heated plasma upward at the local Alfvén speed. When the ejection velocity of the heated plasma exceeds the local sound speed, the sufficiently high pressure of the ejected, heated plasma is expected to enable it to escape from the Sun and form the fast solar wind. In this scenario, no additional coronal heating is required; the local plasma energization through the interchange reconnection suffices to power the fast solar wind. Based on our simulation results, we make a rough estimation of whether the sum of the kinetic and internal energies of the heated plasma ejected by the interchange reconnection is greater than gravitational potential energy. This is evaluated using the expression $\rho_{re}(1/2V_{re}^2 + 1/(\gamma - 1)RT_{re} - GMs/Rs)$. Here, ρ_{re}, V_{re}, and T_{re} represent the density, velocity, and temperature of the ejected, heated plasma at the current sheet, respectively. The adiabatic index $\gamma = 5/3$, and GMs/Rs is the solar gravitational potential. With $V_{re} = \sim 400\ \mathrm{km\ s^{-1}}$ and $T_{re} = \sim 4 \times 10^6$ K, we find that $\rho_{re}(1/2V_{re}^2 + 1/(\gamma - 1)RT_{re} - GMs/Rs)$ is negative. It should be noted that T_{re} is much smaller than the collisionless reconnection-related proton temperature, which is in the range of $\sim$1.0 to $\sim 1.9 \times 10^7$ K (S. D. Bale et al. 2023; J. F. Drake et al. 2023). In this Letter, we primarily focus on how Alfvén waves are excited by the interchange reconnection. Our future research will aim to understand whether and how the heated plasma driven by the interchange reconnection forms the solar wind.

Acknowledgments

The AIA is an instrument on SDO, a National Aeronautics and Space Administration mission. CHIANTI is a collaborative project involving George Mason University (USA), the University of Michigan (USA), and the University of Cambridge (UK). This work is supported by the National Key R&D Program of China (Nos. 2022YFF0503800 and 2021YFA0718600), the National Natural Science Foundation of China (Nos. 42474216, 42274213, 42241118, 12425301), CNSA (No. D050106), and the Climbing Program of NSSC (E4PD3001). D.V. is supported by STFC Consolidated Grants ST/S000240/1 and ST/W001004/1. The work was carried out at National Supercomputer Center in Tianjin, China, and the calculations were performed on TianHe-1 (A).

ORCID iDs

Liping Yang https://orcid.org/0000-0003-4716-2958
Jiansen He https://orcid.org/0000-0001-8179-417X
Xueshang Feng https://orcid.org/0000-0001-8605-2159
Daniel Verscharen https://orcid.org/0000-0002-0497-1096
Fan Guo https://orcid.org/0000-0003-4315-3755
Hui Li https://orcid.org/0000-0003-3556-6568
Hui Tian https://orcid.org/0000-0002-1369-1758
Wenya Li https://orcid.org/0000-0003-1920-2406
Fang Shen https://orcid.org/0000-0002-4935-6679
Chuanpeng Hou https://orcid.org/0000-0001-7205-2449
Mijie Shi https://orcid.org/0000-0002-9201-5896
Honghong Wu https://orcid.org/0000-0003-0424-9228
Ming Xiong https://orcid.org/0000-0001-9427-7366

References

Alfvén, H. 1947, MNRAS, 107, 211
Axford, W. I., & McKenzie, J. F. 1992, in Solar Wind Seven Colloquium, ed. E. Marsch & R. Schwenn (Hoboken, NJ: Wiley), 1
Axford, W. I., McKenzie, J. F., Sukhorukova, G. V., et al. 1999, SSRv, 87, 25
Bale, S. D., Drake, J. F., McManus, M. D., et al. 2023, Natur, 618, 252
Banerjee, D., Teriaca, L., Doyle, J. G., & Wilhelm, K. 1998, A&A, 339, 208
Belcher, J. W., & Davis Leverett, J. 1971, JGR, 76, 3534
Bhattacharjee, A., Huang, Y.-M., Yang, H., & Rogers, B. 2009, PhPl, 16, 112102
Boldyrev, S., & Loureiro, N. F. 2017, ApJ, 844, 125
Chandran, B. D. G., Quataert, E., Howes, G. G., Hollweg, J. V., & Dorland, W. 2009, ApJ, 701, 652
Cheng, X., Li, Y., Wan, L. F., et al. 2018, ApJ, 866, 64
Chitta, L. P., Zhukov, A. N., Berghmans, D., et al. 2023, Sci, 381, 867
Cirtain, J. W., Golub, L., Lundquist, L., et al. 2007, Sci, 318, 1580
Comisso, L., Huang, Y. M., Lingam, M., Hirvijoki, E., & Bhattacharjee, A. 2018, ApJ, 854, 103
Cranmer, S. R. 2012, SSRv, 172, 145
Cranmer, S. R. 2018, ApJ, 862, 6
Daughton, W., Roytershteyn, V., Karimabadi, H., et al. 2011, NatPh, 7, 539
DeForest, C. E. 2004, ApJL, 617, L89
De Pontieu, B., McIntosh, S. W., Carlsson, M., et al. 2007, Sci, 318, 1574
Dere, K. P., Landi, E., Mason, H. E., Monsignori Fossi, B. C., & Young, P. R. 1997, A&AS, 125, 149
Dong, C., Wang, L., Huang, Y.-M., et al. 2022, SciA, 8, eabn7627
Drake, J. F., Agapitov, O., Swisdak, M., et al. 2021, A&A, 650, A2

Drake, J. F., Bale, S. D., Swisdak, M., Raouafi, N. E., & Velli, M. 2023, arXiv:2306.03425
Drake, J. F., Swisdak, M., Schoeffler, K. M., Rogers, B. N., & Kobayashi, S. 2006, GeoRL, 33, L13105
Edmondson, J. K., Lynch, B. J., Antiochos, S. K., De Vore, C. R., & Zurbuchen, T. H. 2009, ApJ, 707, 1427
Emslie, A. G., & Sturrock, P. A. 1982, SoPh, 80, 99
Feng, X., Zhang, S., Xiang, C., et al. 2011, ApJ, 734, 50
Fisk, L. A. 2003, JGRA, 108, 1157
Fisk, L. A., & Schwadron, N. A. 2001, ApJ, 560, 425
Fletcher, L., & Hudson, H. S. 2008, ApJ, 675, 1645
Fu, H. S., Vaivads, A., Khotyaintsev, Y. V., et al. 2017, GeoRL, 44, 37
He, J., Marsch, E., Tu, C., & Tian, H. 2009a, ApJL, 705, L217
He, J., Zhu, X., Yang, L., et al. 2021, ApJL, 913, L14
He, J. S., Tu, C. Y., Marsch, E., et al. 2009b, A&A, 497, 525
Hou, C., He, J., Duan, D., et al. 2024, NatAs, 8, 1246
Huang, Y.-M., & Bhattacharjee, A. 2016, ApJ, 818, 20
Ji, H., Daughton, W., Jara-Almonte, J., et al. 2022, NatRP, 4, 263
Keiling, A. 2024, Alfvén Waves Across Heliophysics: Progress, Challenges, and Opportunities, 304 (Hoboken, NJ: Wiley)
Kigure, H., Takahashi, K., Shibata, K., Yokoyama, T., & Nozawa, S. 2010, PASJ, 62, 993
Lynch, B. J., Edmondson, J. K., & Li, Y. 2014, SoPh, 289, 3043
Ma, Z. W., & Lee, L. C. 1999, JGRA, 104, 10177
Mallet, A., Schekochihin, A. A., & Chandran, B. D. G. 2017, MNRAS, 468, 4862
Mallet, A., Squire, J., Chandran, B. D. G., Bowen, T., & Bale, S. D. 2021, ApJ, 918, 62
Marsch, E., & Mangeney, A. 1987, JGRA, 92, 7363
Mathioudakis, M., Jess, D. B., & Erdélyi, R. 2013, SSRv, 175, 1
McIntosh, S. W., de Pontieu, B., Carlsson, M., et al. 2011, Natur, 475, 477
Moran, T. G. 2001, A&A, 374, L9
Morton, R. J., Tomczyk, S., & Pinto, R. 2015, NatCo, 6, 7813
Morton, R. J., Weberg, M. J., & McLaughlin, J. A. 2019, NatAs, 3, 223
Ofman, L. 2010, LRSP, 7, 4
Osterbrock, D. E. 1961, ApJ, 134, 347
Pariat, E., Antiochos, S. K., & DeVore, C. R. 2009, ApJ, 691, 61
Petschek, H. E., & Thorne, R. M. 1967, ApJ, 147, 1157
Raouafi, N. E., Stenborg, G., Seaton, D. B., et al. 2023, ApJ, 945, 28
Santolík, O., Parrot, M., & Lefeuvre, F. 2003, RaSc, 38, 1010
Shen, C., Chen, B., Reeves, K. K., et al. 2022, NatAs, 6, 317
Sturrock, P. A. 1999, ApJ, 521, 451
Tenerani, A., Velli, M., Matteini, L., et al. 2020, ApJS, 246, 32
Tian, H., DeLuca, E. E., Cranmer, S. R., et al. 2014, Sci, 346, 1255711
Tian, H., McIntosh, S. W., Wang, T., et al. 2012, ApJ, 759, 144
Tomczyk, S., McIntosh, S. W., Keil, S. L., et al. 2007, Sci, 317, 1192
Touresse, J., Pariat, E., Froment, C., et al. 2024, A&A, 692, A71
Tu, C.-Y., & Marsch, E. 1995, SSRv, 73, 1
Tu, C.-Y., Zhou, C., Marsch, E., et al. 2005, Sci, 308, 519
Van Doorsselaere, T., Antolin, P., Yuan, D., Reznikova, V., & Magyar, N. 2016, FrASS, 3, 4
Vasyliunas, V. M. 1975, RvGSP, 13, 303
Wang, L. C., Li, L. J., Ma, Z. W., Zhang, X., & Lee, L. C. 2015, PhLA, 379, 2068
Wang, Y. M. 2020, ApJ, 904, 199
Wyper, P. F., DeVore, C. R., Antiochos, S. K., et al. 2022, ApJL, 941, L29
Yang, L., He, J., Peter, H., et al. 2013a, ApJ, 777, 16
Yang, L., He, J., Peter, H., et al. 2013b, ApJ, 770, 6
Yang, L., He, J., Tu, C., et al. 2017, ApJ, 846, 49
Yang, L., Li, H., Guo, F., et al. 2020a, ApJL, 901, L22
Yang, L., Peter, H., He, J., et al. 2018, ApJ, 852, 16
Yang, L., Zhang, L., He, J., et al. 2015, ApJ, 800, 111
Yang, Z., Bethge, C., Tian, H., et al. 2020b, Sci, 369, 694
Zank, G. P., Nakanotani, M., Zhao, L. L., Adhikari, L., & Kasper, J. 2020, ApJ, 903, 1
Zhao, L. L., Zank, G. P., Adhikari, L., et al. 2022, ApJL, 934, L36
Ziegler, U. 2004, JCoPh, 196, 393